Nanosized MCM-41 silica from rice husk and its application for the removal of organic dyes from water

Giorgio Celoria [1], Federico Begni [1], Geo Paul [1], Stefano Marchesi [1], Enrico Boccaleri [2], Chiara Bisio [1,3]*, Leonardo Marchese [1]

[1] Dipartimento di Scienze e Innovazione Tecnologica, Università del Piemonte Orientale A. Avogadro, viale T. Michel 11, 15121 Alessandria, Italy; giorgio.celoria@uniupo.it (G.C.), federico.begni@uniupo.it (F.B.), geo.paul@uniupo.it (G.P.) stefano.marchesi@uniupo.it (S.M.), chiara.bisio@uniupo.it (C.B.), leonardo.marchese@uniupo.it (L.M.).

[2] Dipartimento per lo Sviluppo Sostenibile e la Transizione Ecologica, Università del Piemonte Orientale A. Avogadro, piazza S. Eusebio 5, 13100 Vercelli, Italy; enrico.boccaleri@uniupo.it, (E.B.).

[3] CNR-SCITEC Istituto di Scienze e Tecnologie Chimiche "Giulio Natta", Via G. Venezian 21, 20133 Milano, Italy; chiara.bisio@uniupo.it (C.B.).

As it can be derived from the PXRD patterns reported in Figure S1, RHA samples are both characterized by amorphous siliceous structures, with a complete lack of a long-range order [1–3]. Moreover, after the acid treatments, the low-intensity reflections within the PXRD pattern of RHA due to metal oxides impurities, typically CaO, Na_2O and K_2O [4–6], have disappeared, suggesting that these phases has been removed upon the acid treatment [7,8].

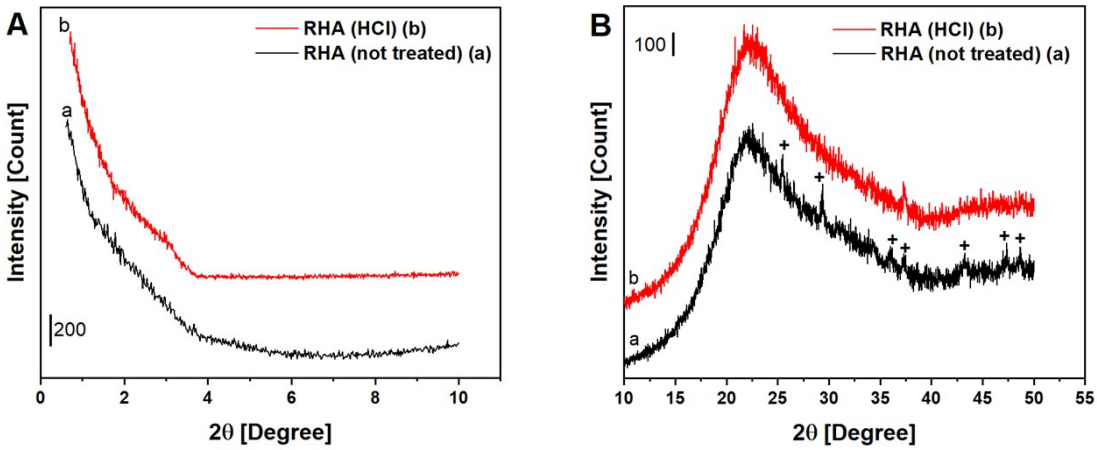

Figure S1. Low-angle (A) and high-angle (B) PXRD pattern of Rice Husk Ashes (RHA) before (a) and after (b) the acid treatment with HCl. Traces of metal oxides within the XRPD patter of the sample before the acid leaching are marked with '+' symbols.

The ATR and FT-IR spectra of RH and RHA samples are reported in Figure S2. The ATR spectrum of RH is characterized by the signals related to the stretching and bending modes of the organic fraction of rice husk,

such as lignin, cellulose and hemicellulose (vide Table S1), whereas, after calcination, the FT-IR spectra of RHA samples show the presence of the typical signals of a silica (vide Figure S2 and Table S2). Moreover, after the acid treatment, the signal related to isolated Si-OH groups appears more intense (vide Figure S2, C), suggesting that, as well as removing the metal oxide impurities, acid treatment might also act as a surface activator.

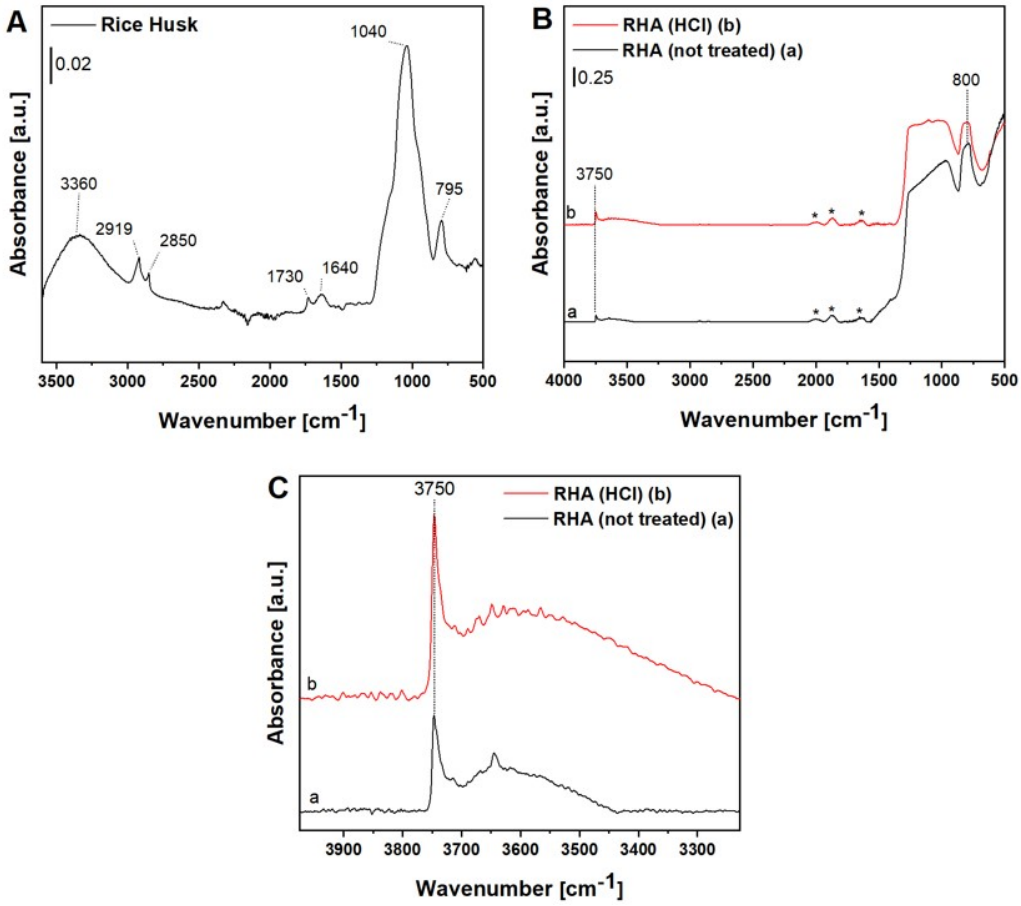

Figure S2. ATR spectrum of Rice Husk (Frame A), FT-IR spectra of rice husk ashes before (a) and after (b) the acid treatment (Frame B and C). Prior to the measurements, the pellets of RHA before and after the acid treatments were treated at beam temperature (35°C) for 1h under vacuum (residual pressure < $2 \cdot 10^{-3}$ mbar). The overtone bands of the siliceous framework are marked with asterisks [9].

Position [cm^{-1}]	Assignment
3360	ν of OH groups [10,11]
2919, 1850	ν_{as} of C-H bonds of CH_2 and CH_3 moieties [10,11]
1730	ν of C=O groups (i.e., carbonyl) [10,11]
1640	ν_{as} of aromatic C=C bonds [10,11]
1040	ν of C-O, C-C-O and ν_{as} of Si-O-Si bonds [10,11]
795	ν modes of Si-O groups of SiO_4 tetrahedra [12,13]

Table S1. FT-IR assignments of rice husk.

Position [cm^{-1}]	Assignment
3750	ν of Si-OH groups [12,13]
3500	ν of H-bonded Si-OH groups [12,13]
1100	ν_{as} of Si-O-Si bonds of SiO_4 tetrahedra [12,13]
800	ν of Si-O groups of SiO_4 tetrahedra [12,13]

Table S2. FT-IR assignments of rice husk ashes before and after the acid treatments

The morphological properties of RHA before and after the acid treatment were investigated through FESEM microscopy. The micrographs of RHA samples are shown in Figure S3. After the acid treatment, RHA are composed by aggregates of smaller round-shape particles.

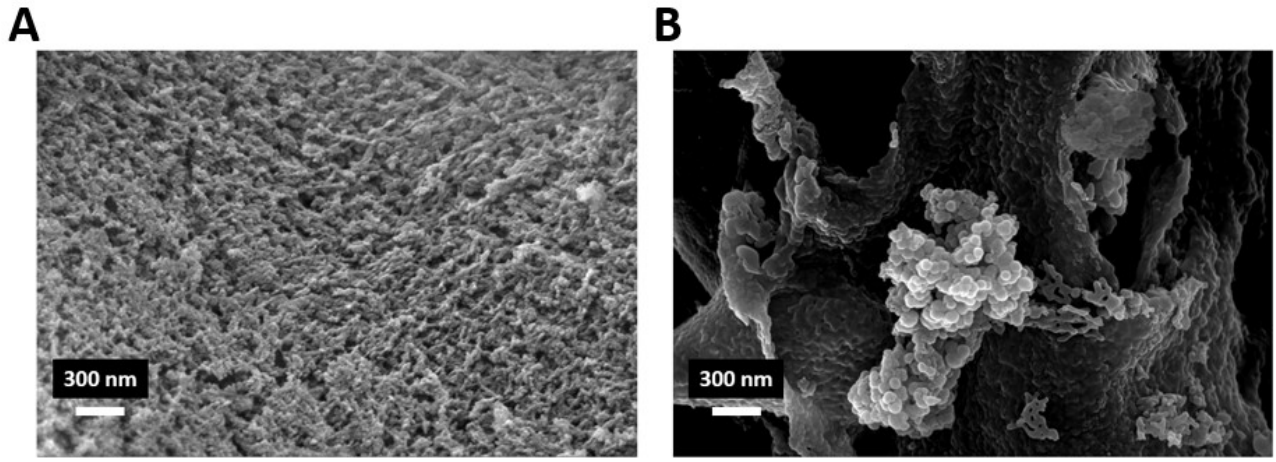

Figure S3. FESEM micrographs of RHA before (A) and after (B) the acid treatment.

The nature of the silicate species within the silicate solution prepared upon the alkaline dissolution of RHA was investigated by means of ^{29}Si NMR spectroscopy. The result of the measurement (vide Figure S4) reveals that amorphous silica within RHA has been mainly solubilized as ortho silicic acid (i.e., $Si(OH)_4$) [14].

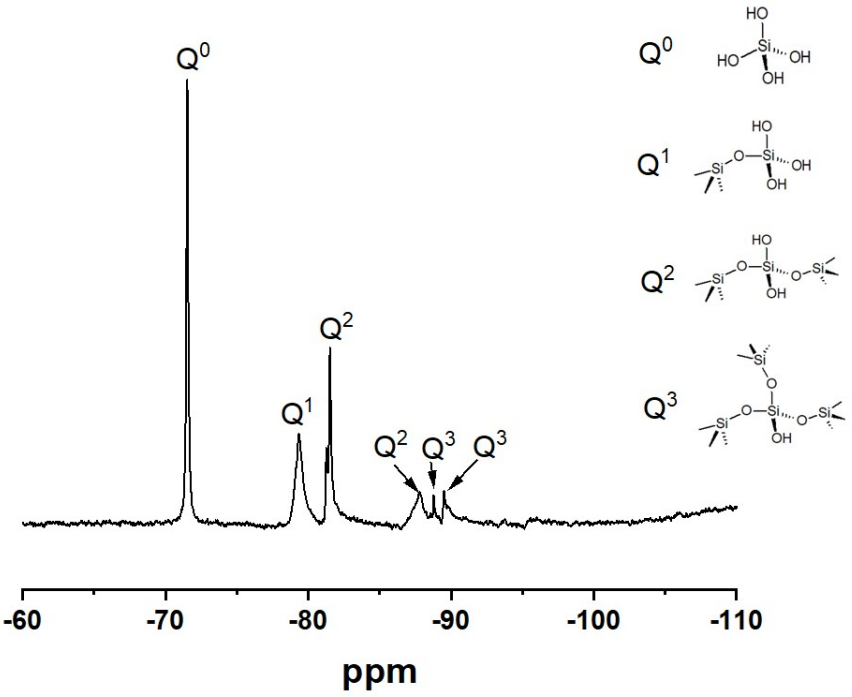

Figure S4. ^{29}Si NMR spectrum of the silicates solution. The different Si nuclei are indicated as Q^n, where n indicate the number of siloxane bond(s) (i.e., Si-O-Si) [14].

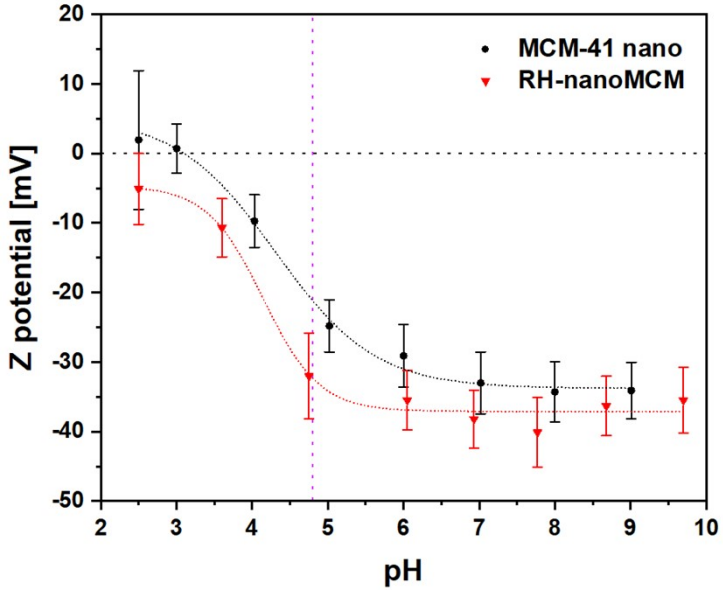

Figure S5. Z-potential in water vs. pH of RH-nanoMCM (triangles) and MCM-41 nano (circles). Error bars represent the standard deviations over three measurements. Horizontal line represents the isoelectric point, whereas the vertical line corresponds to the pH of a $2 \cdot 10^{-1}$ mM Rhodamine B solution.

For pH values below 6, RH-nanoMCM (Figure S5, triangles) is characterized by a Z-potential of ca. -35 mV, thus suggesting that the silanol groups (Si-OH) on the surface of the sample are mainly deprotonated. For pH higher than 6, the Z-potential of RH-nanoMCM increases, until it reaches ca. -5 mV at a pH of 2.5. In that case, the isoelectric point (*i.e.,* when the Z-potential corresponds to 0) has not been reached. In fact, in general, silicas have their isoelectric points at about pH 2 [15,16]. However, the results of the Z-potential measurement

performed on MCM-41 nano (Figure S5, circles) reveal that the isoelectric point of the reference materials is at pH 3.09. Despite that, for pH below 4.5 both RH-nanoMCM and MCM-41 nano behave in a similar manner.

Paragraph S1

The thickness of the silicate walls of RH-nanoMCM and MCM-41 nano was obtained according to the following procedure, reported in C. Vittoni et al. work [17].

According to the Bragg Law ($2d_{hkl}\, sen\theta = n\lambda$), the interplanar distances related to the (100) planes, named d_{100}, of RH-nanoMCM and MCM-41 nano correspond to 39.2 Å and 39.1 Å, respectively.

The distances between the centre of two adjacent pores (a_0) can be obtained from Equation 1, where d_{100} are the previously calculated interplanar distances related to the (100) reflections:

Equation 1: $$a_0 = \sqrt{\frac{4(d_{100})^2}{3}}$$

In the case of RH-nanoMCM, a_0 corresponds to 45.3 Å, whereas for MCM-41 nano a_0 was of 45.1 Å.

Finally, the thickness of the silicate walls (S) of RH-nanoMCM and MCM-41 nano can be calculated from Equation 3, where a_0 is the distance between the centre of two adjacent pores and P_d corresponds to the pore diameter obtained upon the NLDFT analysis (42 Å for RH-nanoMCM and 37 Å for MCM-41 nano).

Equation 2: $$S = |\, a_0 - P_d|$$

From Equation 2, the thickness of the silicate walls of RH-nanoMCM corresponds to 3.3 Å, whereas that of MCM-41 nano is 8.1 Å.

Sample code	Precursor	SSA_{BET} $[m^2 \cdot g^{-1}]$	Total pore volume $[cc \cdot Å^{-1} \cdot g^{-1}]$	Reference
RH-nanoMCM	Rice husk	1050	1.66	This work
MCM-41 nano	TEOS	900	1.68	This work
Nanometric MCM-41 (50 nm)	TEOS	893	1.55	Gatti et al.[18]
MCM-41 nanometric (100-200 nm)	TEOS	1250	0.80	Cara et al. [19]
MCM-41 micrometric (> 200 nm)	TEOS	1060	0.76	Cara et al. [19]
Nanosized MCM-41 (50-70 nm)	TEOS	1050	0.97	Bottinelli et al. [20]
Nanosized MCM-41 (ca. 100 nm)	TEOS	1020	0.93	Cai et al. [21]
Micrometric MCM-41	Rice husk	735	0.77	AbuKhadra et al. [22]
Micrometric MCM-41	Rice husk	848	0.84	Abbas et al. [23]
Micrometric MCM-41	Rice husk	1099	0.96	Bhagiyalakshmi et al. [24]

Table S3. Comparison of the textural properties (i.e., SSA_{BET} and total pore volume) of RH-nanoMCM and MCM-41 nano to those of similar materials reported in the literature. For each sample, it is reported the corresponding reference of the work.

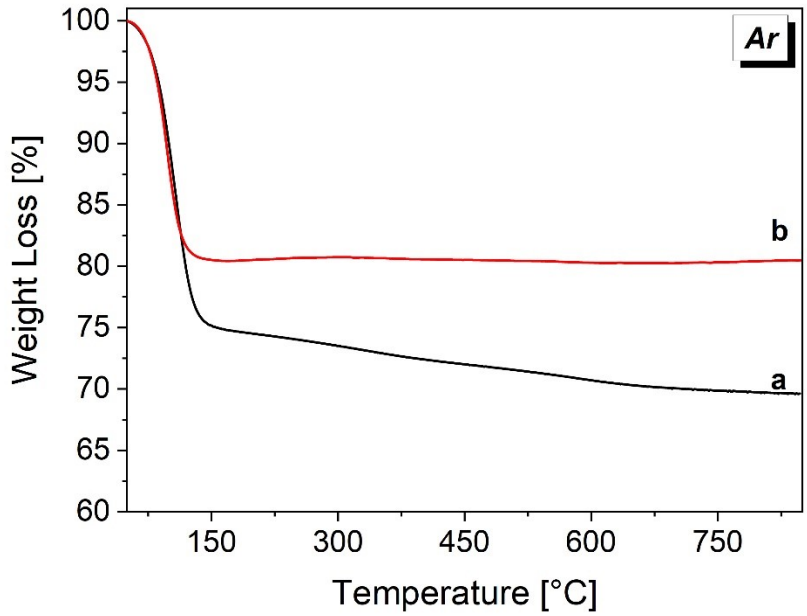

Figure S6. TGA curves of MCM-41 nano (curve a) and RHnanoMCM (curve b). The measurements were performed under inert gas (Ar).

Paragraph S2

According to the procedure used in the literature [25,26], the number of silanols for nm^2 for RH-nanoMCM and MCM-41 nano was estimated from the TGA curves reported in Fig. S6.

The weight loss between 130 and 850 °C (*i.e.,* the dehydroxylation temperature range for silicas [25,26]) was obtained and corresponds to 1.15 g and 5.60 g for RH-nanoMCM and MCM-41 nano, respectively.

Next, the weight losses were converted into g of H_2O/100 g of sample (1.43 g/100g for RH-nanoMCM and 8.04 g/100g for MCM-41 nano), which correspond to 0.001 and 0.004 mol of H_2O/g of RH-nanoMCM and MCM-41 nano, respectively. By means of Avogadro Number, these values were converted into number of Si-OH groups over gram of material (Si-OH/g): $9.56 \cdot 10^{20}$ Si-OH/g for RH-nanoMCM and $5.38 \cdot 10^{21}$ Si-OH/g for MCM-41 nano.

Finally, by exploiting the SSA_{BET} values reported in the main text (vide Table 1), the number of Si-OH groups over nm^2 (Si-OH/nm^2) were obtained.

Si-OH/nm^2 for RH-nanoMCM = 0.91

Si-OH/nm^2 for MCM-41 nano = 5.98

References

1 H. Purwaningsih, Y. Ervianto, V. Mitha Pratiwi, D. Susanti and A. Purniawan, *IOP Conf. Ser. Mater. Sci. Eng.*, 2019, **515**, 012051.
2 G. Ban, S. Song, H. Lee and H. Kim, *Nanomaterials*, 2019, **9**, 300.
3 S. Chandrasekhar, P. N. Pramada and L. Praveen, *J. Mater. Sci.*, 2005, **40**, 6535–6544.
4 L. Fiameni, A. Assi, A. Fahimi, B. Valentim, K. Moreira, G. Predeanu, V. Slăvescu, B. Ş. Vasile, A. I. Nicoară, L. Borgese, G. Boniardi, A. Turolla, R. Canziani and E. Bontempi, *RSC Adv.*, 2021, **11**, 8927–8939.
5 N. Pijarn, A. Jaroenworaluck, W. Sunsaneeyametha and R. Stevens, *Powder Technol.*, 2010, **203**, 462–468.
6 W. H. Kwan and Y. S. Wong, *Mater. Sci. Energy Technol.*, 2020, **3**, 501–507.
7 A. G. Gebretatios, A. R. Kadiri Kanakka Pillantakath, T. Witoon, J.-W. Lim, F. Banat and C. K. Cheng, *Chemosphere*, 2023, **310**, 136843.
8 J. A. Santana Costa and C. M. Paranhos, *J. Clean. Prod.*, 2018, **192**, 688–697.
9 C. Vittoni, G. Gatti, G. Paul, E. Mangano, S. Brandani, C. Bisio and L. Marchese, *ChemistryOpen*, 2019, **8**, 719–727.
10 L. Lazzari, M. Zimmermann, D. Perondi, V. Zampieri, A. Zattera and R. Santana, *Mater. Res.*, DOI:10.1590/1980-5373-mr-2019-0427.
11 M. Morcali, B. Zeytuncu and O. Yucel, *Mater. Res.*, 2013, **16**, 528–538.
12 A. Zecchina, S. Bordiga, G. Spoto, L. Marchese, G. Petrini, G. Leofanti and M. Padovan, *J. Phys. Chem.*, 1992, **96**, 4991–4997.

13 A. Zecchina, S. Bordiga, G. Spoto, L. Marchese, G. Petrini, G. Leofanti and M. Padovan, *J. Phys. Chem.*, 1992, **96**, 4985–4990.
14 H. Jansson, D. Bernin and K. Ramser, *AIP Adv.*, 2015, **5**, 067167.
15 T. P. Goloub, L. K. Koopal, B. H. Bijsterbosch and M. P. Sidorova, *Langmuir*, 1996, **12**, 3188–3194.
16 P. Xu, H. Wang, R. Tong, Q. Du and W. Zhong, *Colloid Polym. Sci.*, 2006, **284**, 755–762.
17 C. Vittoni, G. Gatti, I. Braschi, E. Buscaroli, G. Golemme, L. Marchese and C. Bisio, *Materials*, 2020, **13**, 2690.
18 G. Gatti, C. Vittoni, D. Costenaro, G. Paul, E. Mangano, S. Brandani, L. Marchese and C. Bisio, *Phys. Chem. Chem. Phys.*, 2017, **19**, 29449–29460.
19 C. Cara, E. Rombi, A. Musinu, V. Mameli, A. Ardu, M. Sanna Angotzi, L. Atzori, D. Niznansky, H. L. Xin and C. Cannas, *J. Mater. Chem. A*, 2017, **5**, 21688–21698.
20 E. Bottinelli, I. Miletto, G. Caputo, S. Coluccia and E. Gianotti, *J. Fluoresc.*, 2011, **21**, 901–909.
21 Q. Cai, Z.-S. Luo, W.-Q. Pang, Y.-W. Fan, X.-H. Chen and F.-Z. Cui, *Chem. Mater.*, 2001, **13**, 258–263.
22 M. R. AbuKhadra, A. S. Mohamed, A. M. El-Sherbeeny and M. A. Elmeligy, *J. Hazard. Mater.*, 2020, **389**, 122129.
23 S. H. Abbas, F. Adam and L. Muniandy, *Microporous Mesoporous Mater.*, 2020, **305**, 110192.
24 M. Bhagiyalakshmi, L. J. Yun, R. Anuradha and H. T. Jang, *J. Porous Mater.*, 2010, **17**, 475–484.
25 G. Paul, G. E. Musso, E. Bottinelli, M. Cossi, L. Marchese and G. Berlier, *ChemPhysChem*, 2017, **18**, 839–849.
26 S. Marchesi, F. Carniato, L. Marchese and E. Boccaleri, *ChemPlusChem*, 2015, **80**, 915–918.